Solar Physics (2023) 298:138
https://doi.org/10.1007/s11207-023-02225-3

RESEARCH

Comparison of I-ICME and M-ICME Fittings and In Situ Observation Parameters for Solar Cycles 23 and 24 and Their Influence on Geoeffectiveness

Zhiyong Zhang[1] · Chenglong Shen[1,2] · Yutian Chi[3] · Dongwei Mao[2] · Junyan Liu[2] · Mengjiao Xu[2] · Zhihui Zhong[2] · Can Wang[2] · Yuming Wang[1,2]

Received: 6 May 2023 / Accepted: 28 October 2023 / Published online: 27 November 2023

Abstract

To understand the weaker geomagnetic activity in Solar Cycle 24, we present comparisons of interplanetary coronal mass ejections (ICMEs) fittings and in situ observation parameters in Solar Cycles 23 and 24. According to their in situ features, ICMEs are separated into two categories: isolated ICMEs (I-ICMEs) and multiple ICMEs (M-ICMEs). The number of I-ICMEs in Solar Cycles 23 and 24 does not show a strong difference, while the number of M-ICMEs, which have a high probability of causing intense geomagnetic storms, declines proportionally to the sunspot number in Solar Cycle 24. Despite no obvious variation in their distribution, the geoeffective ICMEs in Solar Cycle 23 have a larger average total magnetic field strength and a larger southern magnetic field than those of Solar Cycle 24. Since the average solar wind velocities of the two solar cycles differ, the geoeffective ICMEs in Solar Cycle 23 have a higher velocity and distinct speed distributions from those in Solar Cycle 24. The total magnetic flux and radius of I-ICMEs in Solar Cycle 23 are larger than those in Solar Cycle 24, while the axial magnetic field intensity is basically the same. We propose that geomagnetic activity in Solar Cycle 24 is lower than that of Solar Cycle 23, due to the smaller M-ICME number, the slower ICME speed, and absence of ICME events with significant southward magnetic field.

Keywords Interplanetary coronal mass ejection · Flux rope · Geomagnetic storm

✉ C. Shen
clshen@ustc.edu.cn

✉ Y. Chi
ytchi@mail.ustc.edu.cn

1 Deep Space Exploration Laboratory/School of Earth and Space Sciences, University of Science and Technology of China, Hefei 230026, China

2 CAS Center for Excellence in Comparative Planetology/CAS Key Laboratory of Geospace Environment/Mengcheng Geophysics National Observation and Research Station, University of Science and Technology of China, Hefei 230026, China

3 Institute of Deep Space Sciences, Deep Space Exploration Laboratory, Hefei 230026, China

1. Introduction

Coronal mass ejections (CMEs) are large amounts of magnetized plasma that the Sun ejects into the interplanetary space (Aulanier, 2010; Gulisano et al., 2012; Mierla et al., 2010; Vourlidas, 2014; Zhang et al., 2021). Their interplanetary counterparts are usually referred to as the interplanetary coronal mass ejections (ICMEs) (Fadaaq and Badruddin, 2021; Mustajab and Badruddin, 2011; Plunkett et al., 2001; Richardson and Cane, 2012; Russell, Shinde, and Jian, 2005; Zhang et al., 2021; Chi et al., 2016). ICMEs may have a southward component of the interplanetary magnetic field, so they are generally considered to be the main interplanetary structures that may cause geomagnetic storms (Echer et al., 2008; Gonzalez et al., 1994, 2007, 2011; Wang et al., 2002; Xue et al., 2005; Zhang et al., 2003). The maximum value of the southward magnetic field is an important factor determining the geoeffectiveness of ICMEs (Echer et al., 2008; Shen et al., 2017; Gonzalez et al., 2011). The interaction between two CMEs, as well as the interaction between an ICME and a shock wave, can affect the strength of the southward magnetic field carried by the combined ICME (Shen et al., 2017; Xu et al., 2019; Lugaz et al., 2017; Lugaz, Manchester, and Gombosi, 2005), usually (although not always) enhancing the southward magnetic field. There is a special class of ICMEs called magnetic clouds. The observed characteristics of magnetic clouds are the enhancement of the magnetic field intensity, a large and smooth rotation of the magnetic field direction, and a low plasma β value (Burlaga et al., 1981; Klein and Burlaga, 1982). It is usually considered as a kind of annular magnetic flux rope with the two ends sometimes connected to the Sun (Burlaga et al., 1981; Janvier, Démoulin, and Dasso, 2013; Larson et al., 1997). The fitted models of ICMEs include cylindrical symmetric force-free flux rope models (Burlaga, 1988; Goldstein, 1983; Kumar and Rust, 1996; Lepping, Jones, and Burlaga, 1990; Marubashi, 1986; Wang et al., 2015), cylindrical asymmetric (non-) force-free flux rope models (Cid et al., 2002; Hidalgo, Nieves-Chinchilla, and Cid, 2002; Hidalgo et al., 2002; Hu and Sonnerup, 2002; Mulligan and Russell, 2001; Vandas and Romashets, 2003), and toroidal flux rope models (Hidalgo and Nieves-Chinchilla, 2012; Marubashi and Lepping, 2007; Romashets and Vandas, 2003). In this article, we use the velocity-modified cylindrical force-free flux rope model proposed by Wang et al. (2015). It was developed from the cylindrical symmetric force-free flux rope model, but considers the linear propagation, expansion, and polar motion of the plasma.

With the coming of the space era, people have paid increasing attention to space weather events, so geomagnetic storms have been widely studied (Echer et al., 2008; Echer, Tsurutani, and Gonzalez, 2013; Qiu et al., 2022; Yermolaev et al., 2021; Zhang et al., 2007; Shen et al., 2017). Solar Cycle 23 (1996-2008) produced 303 geomagnetic storms, including 213 moderate geomagnetic storms (-100 nT $< \mathrm{Dst_{min}} \leq -50$ nT), 72 strong geomagnetic storms (-200 nT $< \mathrm{Dst_{min}} \leq -100$ nT), and 18 extremely strong geomagnetic storms ($\mathrm{Dst_{min}} \leq -200$ nT) (Echer et al., 2008; Echer, Tsurutani, and Gonzalez, 2013). However, in Solar Cycle 24 (2009–2019), there were only 149 geomagnetic storms, including 127 moderate geomagnetic storms, 20 strong geomagnetic storms, and 2 extremely strong geomagnetic storms (Qiu et al., 2022). Solar Cycle 24 is the weakest one during the space age until now (Hajra et al., 2021; Zhang et al., 2021), geomagnetic storms are weaker and fewer than in Solar Cycle 23. Many researchers are interested in the reason for the difference in geomagnetic storms between these two solar cycles (Gopalswamy et al., 2014, 2015b; Hajra et al., 2021; Rawat, Echer, and Gonzalez, 2018). The goal of this research is to compare the interplanetary coronal mass ejections fitting parameters and observational data characteristics in Solar Cycles 23 and 24 to figure out why the geomagnetic storms during Solar Cycle 24 are so weak and rare.

The layout of the article is as follows, Section 2 introduces the data used in this study and the classification criteria of ICMEs. Section 3 contains the comparison of magnetic field and solar wind data between Solar Cycles 23 and 24. A summary of our main results and a discussion are presented in Section 4.

2. Data and Methods

We identified ICMEs based on local data of plasma and magnetic field. We have adopted the criteria of Shen et al. (2014, 2017) and Chi et al. (2016), as follows: i) enhanced magnetic field intensity, ii) steady change of the magnetic field direction, iii) decreased solar wind velocity, iv) lower proton temperature relative to background solar wind, and v) lower plasma β value relative to the background solar wind. If a structure meets three or more of these criteria, it is identified as an ICME. The list of interplanetary coronal mass ejections in Solar Cycles 23 and 24 in this study is from http://space.ustc.edu.cn/dreams/wind_icmes/index.php (Chi et al., 2016), interplanetary magnetic field and solar wind data are from *Wind* and the *Advanced Composition Explorer* (ACE) satellites (https://cdaweb.gsfc.nasa.gov/istp_public/). The sunspot number data version 2.0 are from the World Data Center-Sunspot Index and Long-term Solar Observations (WDC-SILSO), Royal Observatory of Belgium, Brussels (https://wwwbis.sidc.be/silso/datafiles). The simulation of the velocity-modified cylindrically symmetric force-free flux rope model can be obtained from http://space.ustc.edu.cn/dreams/mc_fitting/ (Wang et al., 2015).

During the propagation of ICMEs from the Sun to Earth, they may interact with each other. Therefore, in situ observations of ICMEs always show different characteristics. In this study, we used the classification criteria of Shen et al. (2017) to divide ICMEs into two categories: multiple ICMEs (M-ICMEs) and isolated ICMEs (I-ICMEs).

1. The classification criteria for multiple ICMEs are as follows. i) The interval between ICMEs is less than 6 hours, in which case we believe that these ICMEs may have interactions, as shown in Figure 1. ii) The shock wave driven by the following ICME propagated into the ejecta region of the preceding ICME, in this case, we believe that the preceding ICME interacted with the shock (Shen et al., 2018; Xu et al., 2019). There is a situation in which a shock is observed, but the ICME causing this shock is not observed, as shown in Figure 2. This is because the width of the shock wave is wider than the width of the ICME or the ICME is deflected during propagation. iii) An ICME has been studied by other researchers and is believed to be formed by two magnetic clouds (Dasso et al., 2009) or to be part of the merged interction region (Burlaga et al., 2003; Chi et al., 2021). There are 71 groups of M-ICMEs (148 M-ICMEs), of which 52 groups (109 M-ICMEs) happened in Solar Cycle 23 and 19 groups (39 M-ICMEs) in Solar Cycle 24.

   Figure 1 shows a typical group of M-ICMEs events (interaction between ICME and ICME): the 1 – 2 February 2003 event and the 2 – 3 February 2003 event. The first shaded area in Figure 1 is the body area of the first ICME, which began at 18:49 UT on 1 February 2003 and ended at 13:07 UT on 2 February 2003. About 3 hours later, the second ICME was observed by the *Wind* satellite. This ICME began at 16:16 UT on 2 February 2003 and ended at 07:27 UT on 3 February 2003. Between the two ICMEs, the in situ data show the characteristics of the interaction region: the magnetic field intensity is low, the proton number density increases, and the proton temperature increases (Wang, Ye, and Wang, 2003; Wang et al., 2005). The group of M-ICMEs events caused a moderate geomagnetic storm with $\mathrm{Dst}_{\mathrm{min}} = -72$ nT.

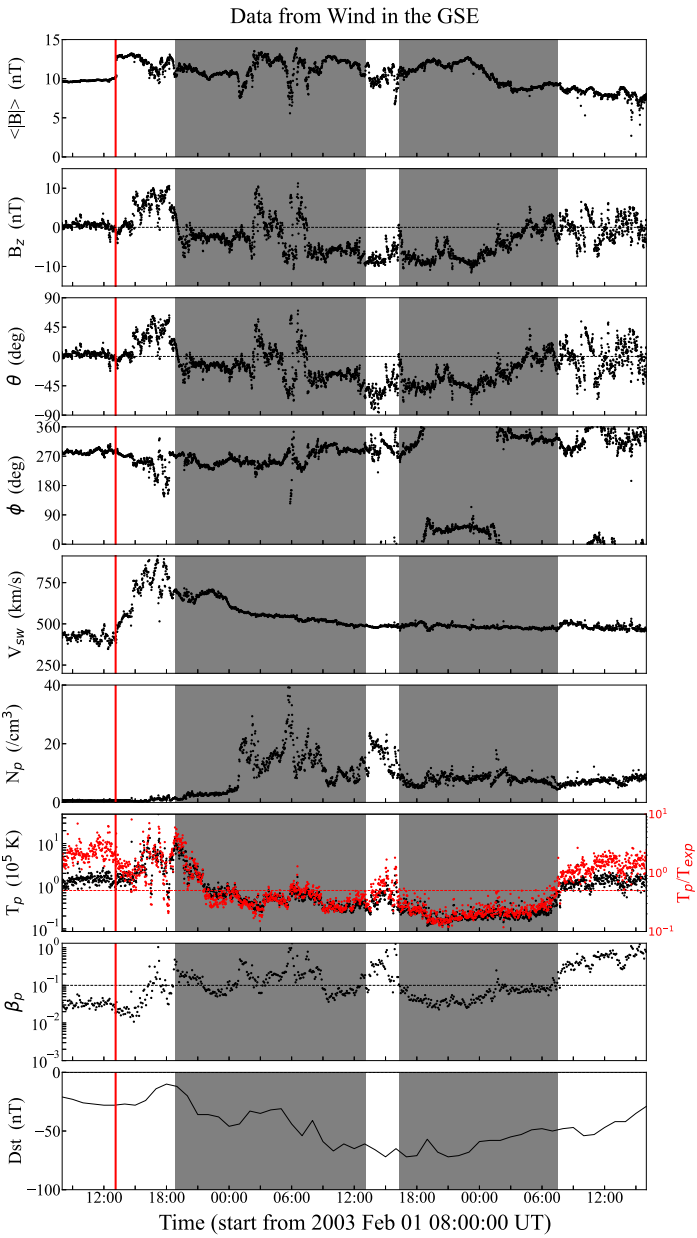

Figure 1 An example of a group of M-ICMEs (interaction between ICME and ICME): the 1 – 2 February 2003 event and the 2 – 3 February 2003 event. From *top to bottom*, panels are the magnetic field strength ($< |B| >$), z-component of the magnetic field in the GSE coordinate system (B_z), the elevation (θ) and azimuthal (ϕ) angles of the magnetic field direction in the GSE coordinate system, solar wind speed (V_{sw}), proton density (N_p), proton temperature (T_p), the ratio of proton thermal pressure to magnetic pressure (β_p), and the Dst index. The *shaded area* represents the body of the ICMEs. The *red vertical line* shows the time of the shock driven by the first ICME.

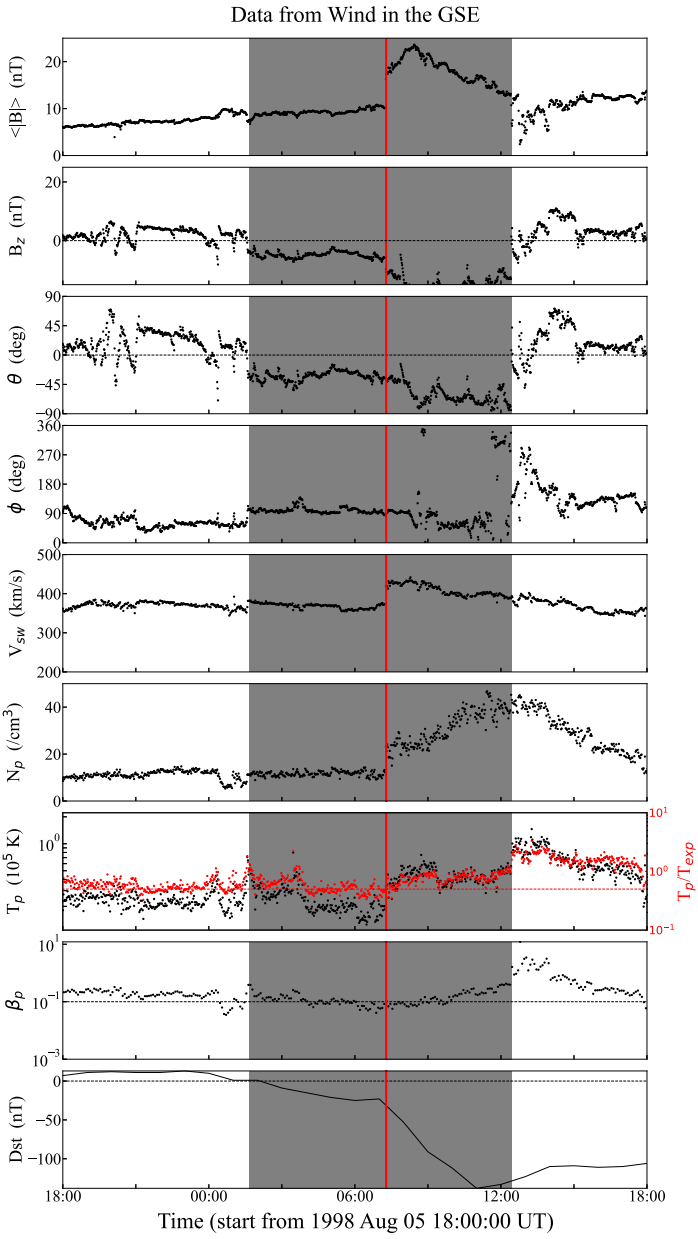

Figure 2 An example of the M-ICMEs (ICME interacts with shock): the 6 August 1998 event. From *top to bottom*, panels are the magnetic field strength ($< |B| >$), z-component of the magnetic field in the GSE coordinate system (B_z), the elevation (θ) and azimuthal (ϕ) angles of the magnetic field direction in the GSE coordinate system, solar wind speed (V_{sw}), proton density (N_p), proton temperature (T_p), the ratio of proton thermal pressure to magnetic pressure (β_p), and the Dst index. The *shaded area* represents the body of the ICMEs. The *red vertical line* shows the time of the shock driven by the ICME.

Figure 2 shows a typical M-ICME event (ICME interacts with shock): the 6 August 1998 event. It began at 01:38 UT on 6 August 1998 and ended at 12:25 UT on the same day. While the ICME was passing through the *Wind* satellite, a shock wave reached at 07:17 UT on 6 August 1998 (as shown by the red vertical solid line). This shock compressed the ICME and significantly increased its magnetic field strength, solar wind speed, proton number density, and proton temperature. This ICME is associated with a strong geomagnetic storm. The peak of the Dst index of this geomagnetic storm is −138 nT.

2. An isolated ICME is one that is not affected by other CMEs. It is the simplest ICME structure. There are 285 I-ICMEs, including 144 in Solar Cycle 23 and 141 in Solar Cycle 24. Figure 3 shows an example of a typical I-ICME event: the 28 – 29 October 2000 event. From 22:23 UT on 28 October 2000 to 23:21 UT on 29 October 2000 (gray shade), in situ observations showed enhanced magnetic field strength, smooth rotation of the magnetic field direction, decreased speed, low proton temperature, and low plasma beta. This ICME fulfills all our ICME criteria (i, ii, iii, iv, and v). Approximately 11 hours before the ICME start time, a shock wave driven by this ICME (red vertical solid line in Figure 3) was detected. This ICME is an interplanetary source of a strong geomagnetic storm.

There are ICMEs that are classified neither as I-ICMEs nor as M-ICMEs because they are controversial. If analyzed using only data from one satellite, they may be I-ICMEs, but if analyzed using multi-satellite data, they may be M-ICMEs (Shen et al., 2021; Lugaz et al., 2017; Chi et al., 2018). These are ICMEs lasting more than 30 hours and fast ejectas (non-magnetic clouds with a duration of more than 24 hours and a maximum speed of more than 600 km s^{-1}), we do not consider these ICMEs in the comparison discussed below. Then, we used the velocity-modified cylindrical force-free flux rope model to fit the I-ICMEs. We used the parameters of closest approach distance (d) and normalized root mean square (χ_n) to judge the fitting quality. Table 1 presents the specific meanings of the parameters. Finally, according to Lepping et al. (2006) and Wang et al. (2015), we only retain $|d| < 0.97$ and $\chi_n < 0.5$ fitting events, only 207 I-ICMEs, including 104 events in Solar Cycle 23 and 103 events in Solar Cycle 24.

We used the Kolmogorov–Smirnov test (KS test) to compare the ICME parameters in Solar Cycles 23 and 24. The KS test is a non-parametric test method, in which the distribution function of the data set to be tested does not need to be known. It was used to test data sets of physical parameters of magnetic clouds and the surrounding heliosphere (Gopalswamy et al., 2015a), as well as CME angular width and speed data sets (Gopalswamy et al., 2014). The two-sample KS test is to see if two independent samples come from the same distribution. The statistic of the two-sample KS test is: $D_{n_{23},n_{24}} = sup_x|F_{23,n_{23}}(x) - F_{24,n_{24}}(x)|$ or $D_{n_{23},n_{24}} = sup_x|F'_{24,n_{24}}(x) - F'_{23,n_{23}}(x)|$. D is the maximum deviation of the empirical cumulative distribution function between the two samples. F is an empirical cumulative distribution function (CDF), which represents the probability that a random variable X is less than or equal to x ($F_X(x) = P(X \leq x)$). F' is an empirical complementary cumulative distribution function (CCDF), which represents the probability that a random variable X is greater than x ($F'_X(x) = P(X > x)$, $F'_X = 1 - F_X$). n is the sample size and sup is an upper bound function. The KS test generally has two hypotheses, the null hypothesis and the alternative hypothesis. The null hypothesis assumes that the two samples come from the same distribution, and the alternative hypothesis assumes that the two samples come from different distributions. If $D_{n_{23},\ n_{24}} > D_{crit,\alpha} = \sqrt{-ln(\frac{\alpha}{2}) \times \frac{1}{2}} \times \sqrt{\frac{n_{23}+n_{24}}{n_{23} \times n_{24}}}$, then the null hypothesis is rejected at α level, where α is the significance level. When α is given, the larger

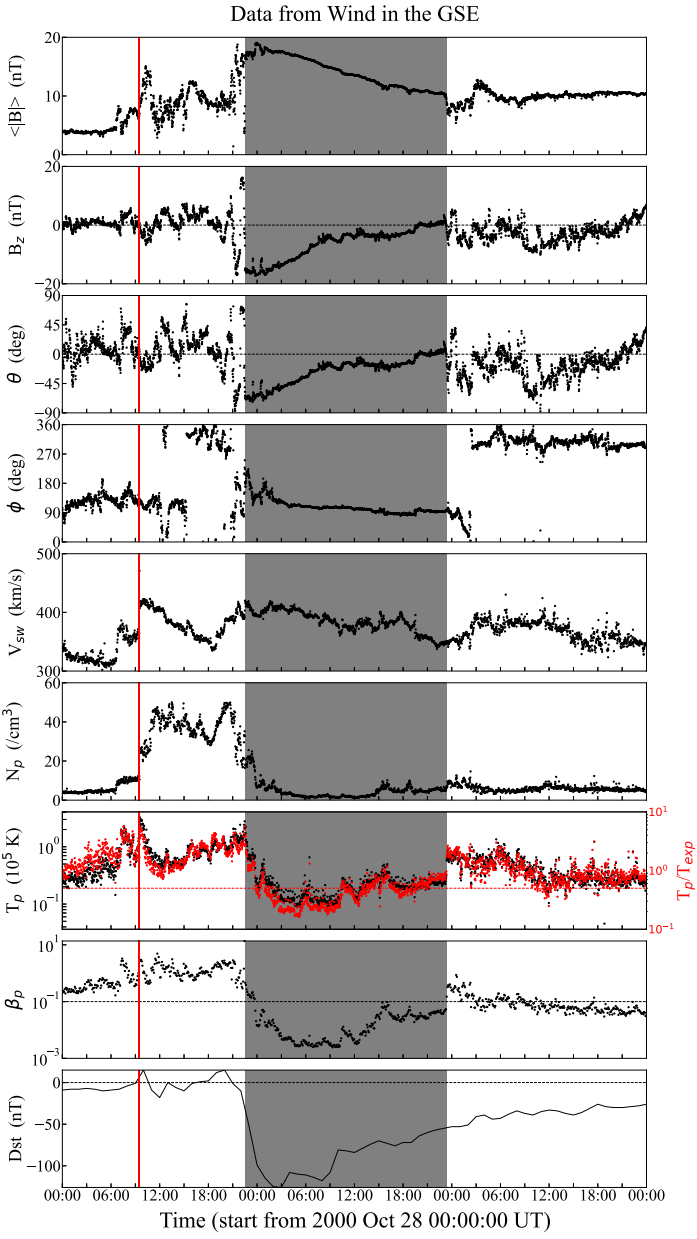

Figure 3 An example of the I-ICMEs: the 28 – 29 October 2000. From *top to bottom*, panels are the magnetic field strength ($<|B|>$), z-component of the magnetic field in the GSE coordinate system (B_z), the elevation (θ) and azimuthal (ϕ) angles of the magnetic field direction in the GSE coordinate system, solar wind speed (V_{sw}), proton density (N_p), proton temperature (T_p), the ratio of proton thermal pressure to magnetic pressure (β_p), and Dst index. The *shaded area* represents the body of the ICMEs. The *red vertical line* shows the time of the shock driven by the ICME.

Table 1 Parameters of the velocity-modified cylindrical force-free flux rope model.

Parameter	Explanation
t_c	The time when the satellite arrived at the closest approach.
B_0	The magnetic field intensity at the flux rope axis at the time of t_c.
R	The radius of the cross section of the flux rope at the time of t_c.
Φ_t	The total magnetic flux of the flux rope.
d	The closest approach distance of the observational path to the axis of the flux rope.
χ_n	The normalized root mean square of the difference between the modeled results and observations.

the sample size, the more sensitive the minimum bound. $D_{n_{23},n_{24}} > D_{crit,\alpha}$ is equivalent to $P < \alpha$, with $P = 2e^{-2(D_{n_{23},n_{24}})^2 \frac{n_{23} \times n_{24}}{n_{23}+n_{24}}}$. In the KS test, the absolute size of the P value is not worth noting, but rather its relative size. In this article, we took the $\alpha = 0.10$ level, that is, if the P-value is greater than 0.10, we consider the distribution of the two samples not to be different. If there is no difference in the distribution of two independent samples, the two distribution curves (CDF or CCDF) match perfectly in the best case.

3. Results and Analysis

3.1. ICMEs and Sunspot Number

Previous research has found a strong association between the number of sunspots and CMEs (Gopalswamy et al., 2010; Webb and Howard, 1994). ICMEs are the interplanetary counterparts of CMEs, which should also have a good correlation with the sunspot number. The distribution of the annual sunspot number and annual ICME number from 1996 to 2019 is shown in Figure 4. As shown in panel a in Figure 4, although there is a difference in peak time, the distribution of ICMEs and sunspot number are extremely similar with one another. The correlation coefficient between ICME number and sunspot number is r = 0.81, which explains why there are more ICMEs in Solar Cycle 23 than in Solar Cycle 24. We also discussed the relationship between M-ICMEs and I-ICMEs and sunspot number. We found that M-ICMEs are mainly present during the solar maximum period, 47.7% during Solar Cycle 23 and 48.7% during Solar Cycle 24. Not surprisingly, there is a good correlation (r = 0.81) between the M-ICMEs and the sunspot number, as shown in panel b. In panel c, we found that in general, the correlation between the I-ICMEs and the sunspot number is weak (r = 0.46), but when the sunspot number is less than 90, the correlation between the I-ICMEs and the sunspot number is strong (r = 0.86). We believe this is because, as the sunspot number increases, the frequency of CME eruptions reaches a high level and the time interval between eruptions becomes smaller and smaller, so the probability of isolated CMEs actually decreases, as shown in Figure 5. We also classified ICMEs according to the B_z-profiles or θ_B-profiles (θ_B is the elevation of the field direction in the GSE coordinate system from *Wind*), which is important because we are finally interested in the magnetic reconnection between ICMEs and the Earth's magnetosphere (Lepping, Wu, and Berdichevsky, 2005; Zhang and Burlaga, 1988). In Table 2, we qualitatively defined 13 different ICME types (Lepping et al., 2006). Figure 6 shows an example of the B_z-profiles for these ICMEs types. In Figure 6 a–g, these types of ICMEs with long-lasting southward

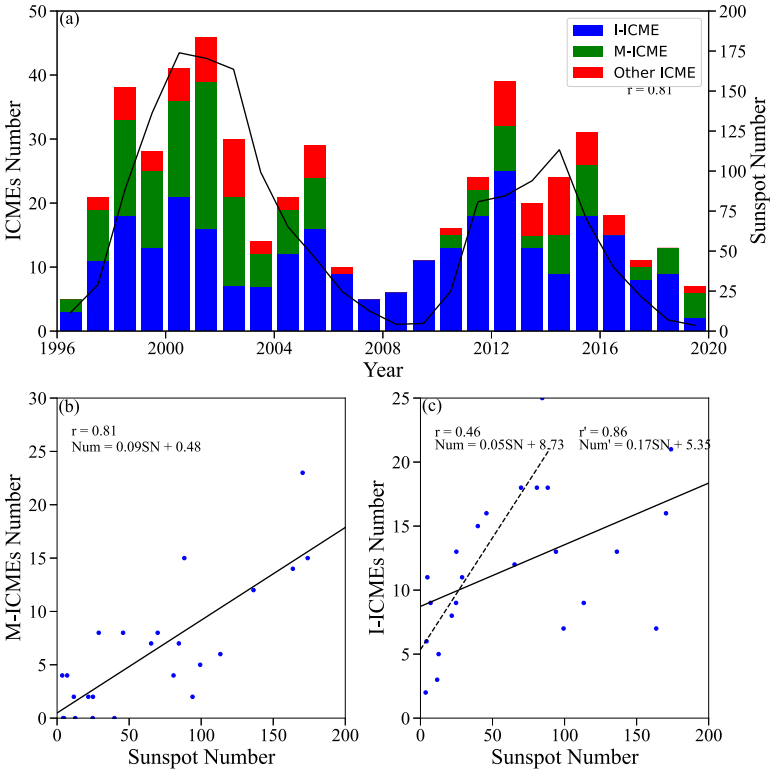

Figure 4 (**a**) Annual ICME number and sunspot number distribution. The *blue column* represents the number of I-ICMEs per year, the *green column* represents the number of M-ICMEs per year, and the *red column* represents the number of other ICMEs per year. (**b**) The relationship between the annual M-ICMEs and the sunspot number. (**c**) The relationship between the annual I-ICMEs and the sunspot number. r is the correlation coefficient between the M-ICME and I-ICME number and the sunspot number in general, and r' is the correlation coefficient between the I-ICME number and the sunspot number when the sunspot number is less than 90.

Figure 5 Monthly CMEs and sunspot number distribution. The CME number only counts CMEs with width $\geq 30°$.

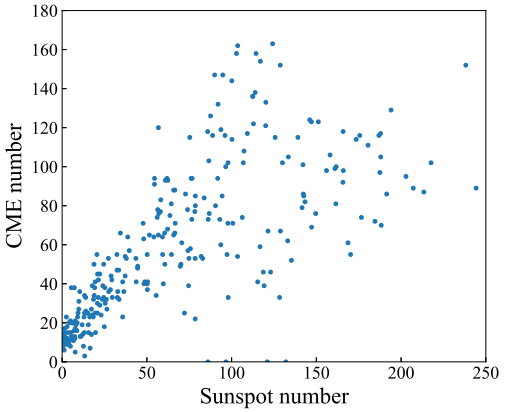

Table 2 Types and number of ICMEs.

Category	Definition	Number	
		Solar Cycle 23	Solar Cycle 24
0	Complex	27	19
1	N → S	33	27
11	S → N	33	25
2	N → S, mostly N	12	8
12	S → N, mostly S	21	9
3	Almost all N	31	30
13	Almost all S	33	33
4	All N	28	12
14	All S	21	15
5	N → S, mostly S	20	13
15	S → N, mostly N	12	6
6	N → S → N	9	12
16	S → N → S	14	5
Total number		294	214

Category 0: The direction of B_z changes several times.

Category 1 (Category 11): B_z can be divided into two parts with roughly the same time scale, the first part is the northward (southward) magnetic field, and the second part is the southward (northward) magnetic field.

Category 2 (Category 12): B_z can be divided into two parts with different time scales. The first part is the northward (southward) magnetic field with large time scale, and the second part is the southward (northward) magnetic field with small time scale.

Category 3 (Category 13): B_z is almost entirely northward (southward).

Category 4 (Category 14): B_z is all northward (southward).

Category 5 (Category 15): B_z can be divided into two parts with different time scales. The first part is the northward (southward) magnetic field with small time scale, and the second part is the southward (northward) magnetic field with large time scale.

Category 6 (Category 16): B_z can be divided into three parts with roughly the same time scale. The first part is the northward (southward) magnetic field, the second part is the southward (northward) magnetic field, and the third part is the northward (southward) magnetic field.

magnetic field are called the most geoeffective ICMEs; due to the rotation of the magnetic field, the electromagnetic coupling between these ICMEs and the Earth's magnetosphere is expected to be the most geoeffective. We consider them to be important sources of geomagnetic storms, in Sections 3.3 we only compare the parameters of these eight types of ICMEs. During Solar Cycle 23, there were 184 ICMEs in these eight categories, of which 93 were I-ICMEs and 68 were M-ICMEs, while there were only 139 in Solar Cycle 24, of which 94 were I-ICMEs and 25 were M-ICMEs. Although they differ greatly in number, the proportion of I-ICMEs and M-ICMEs in both solar cycles is very similar (64.6% for I-ICMEs and 62.4% for M-ICMEs in Solar Cycle 23, and 66.7% for I-ICMEs and 64.1% for M-ICMEs in Solar Cycle 24). The number of the most geoeffective I-ICMEs in the two solar cycles is basically the same, but the number of the most geoeffective M-ICMEs in Solar Cycle 23 is more than twice that in Solar Cycle 24. In addition, we also compared the number of ICMEs with N → S (including categories 1, 2, 5) and S → N (including categories 11, 12, 15) in Solar Cycles 23 and 24. We found that no matter in which solar cycle, the number of ICMEs with N → S and S → N is basically the same.

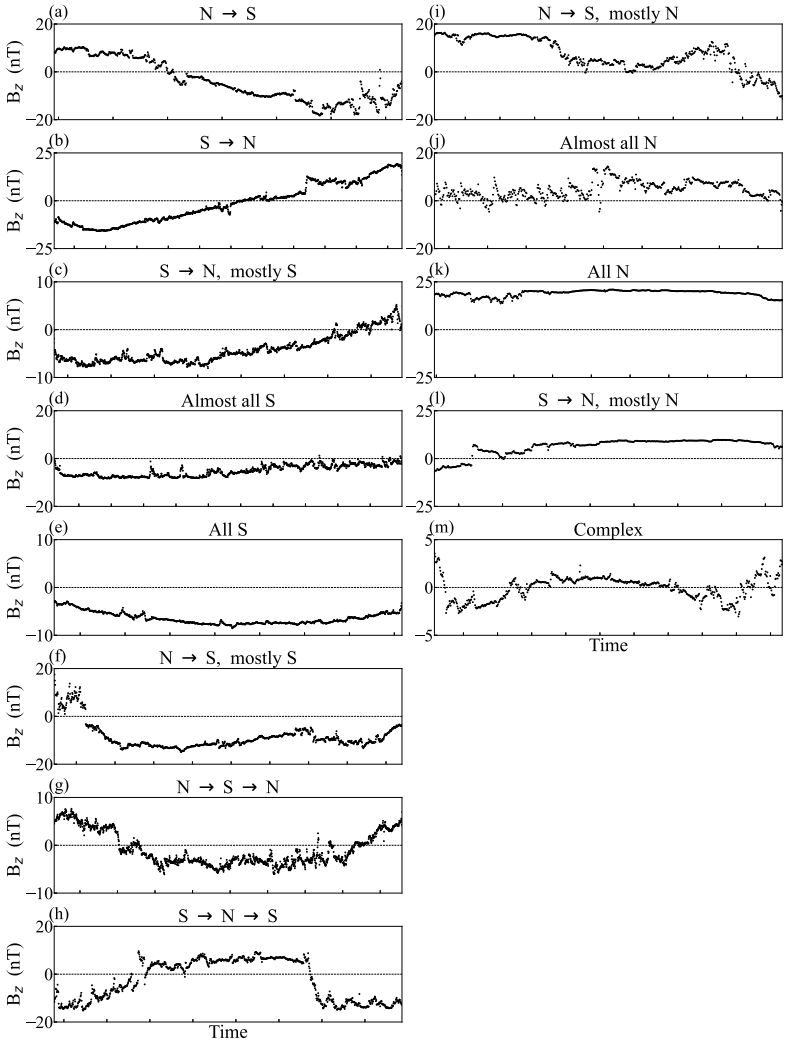

Figure 6 An example of B_z-profiles for 13 ICME types. Panels $a-g$ show that the ICME has a long-lasting southward magnetic field, known as the most geoeffective ICMEs.

3.2. Total Magnetic Flux, Radius, and Axial Magnetic Field Intensity

In order to verify that the size of ICMEs of Solar Cycle 24 is smaller than that of Solar Cycle 23 (Gopalswamy et al., 2015a) and to avoid that the ICME width calculated by local single-point observation may have different results, depending on the satellite passing through different parts of the ICMEs, we used the model proposed by Wang et al. (2015) to calculate the radius of the ICMEs. Then, we compared the radius (R) of I-ICMEs for Solar Cycles 23 and 24, in addition to their total magnetic flux (Φ_t) and axial magnetic field intensity (B_0). Table 3 shows their average and median values and Figure 7 shows their distributions. From Table 3, we found that the total magnetic flux and radius of I-ICMEs in Solar Cycle 23 were greater than those in Solar Cycle 24 and the axial magnetic field intensity in these two

Table 3 Comparison of the results of some ICMEs parameters in Solar Cycles 23 and 24.

	Average values			Median values		
	SC 23	SC 24	ratio	SC 23	SC 24	ratio
SN	78.82	49.51	0.63	/	/	/
Φ_t (10^{21} Mx)[i]	4.16	2.67	0.64	2.80	1.92	0.69
R (AU)[i]	0.095	0.072	0.75	0.080	0.064	0.80
B_0 (nT)[i]	16.46	15.67	0.95	13.66	14.25	1.04
$\|B\|_{ave}$ (nT)[ii]	11.17	9.82	0.88	10.14	8.87	0.87
Bs_{max} (nT)[ii]	11.71	8.80	0.75	9.53	8.04	0.84
V_{ave} ($km\ s^{-1}$)[ii]	458.15	405.68	0.89	441.46	390.99	0.89
$\|B\|_{ave}$ (nT)[iii]	13.54	10.26	0.76	10.70	8.57	0.80
Bs_{max} (nT)[iii]	15.41	11.67	0.76	11.35	8.20	0.72
V_{ave} ($km\ s^{-1}$)[iii]	489.30	457.88	0.94	471.14	403.17	0.86

SC: solar cycle.

SN: sunspot number.

Φ_t: the I-ICME total magnetic flux.

R: the I-ICME radius.

B_0: the I-ICME axial magnetic field intensity.

$|B|_{ave}$: the average value of total magnetic field intensity of the most geoeffective categories of ICMEs.

Bs_{max}: the maximum value of south magnetic field intensity of the most geoeffective categories of ICMEs.

V_{ave}: the average propagation speed of the most geoeffective categories of ICMEs.

[i]ICME parameters obtained by fitting.

[ii]Parameters derived from the most geoeffective categories in I-ICMEs.

[iii]Parameters derived from the most geoeffective categories in M-ICMEs.

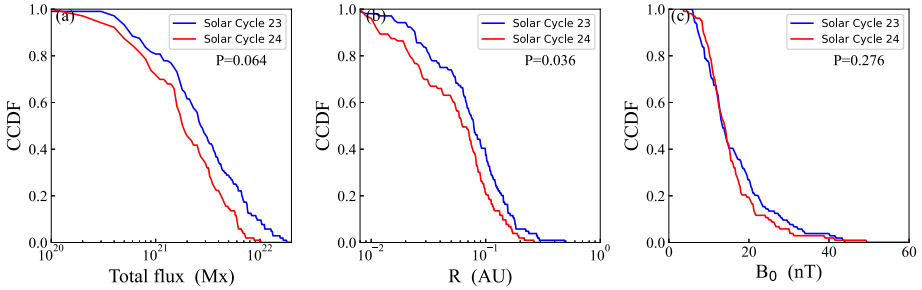

Figure 7 Distribution of the total magnetic flux, radius, and axial magnetic field intensity. The *solid blue line* in the figure represents Solar Cycle 23, while the *red line* represents Solar Cycle 24. The CCDF is a complementary cumulative distribution function and the P-value is the result of the KS test.

cycles had little difference. From Figure 7, we can see the following. 1) The complementary cumulative distribution function (CCDF) of the total magnetic flux of I-ICMEs in Solar Cycle 23 is almost above the CCDF of the total magnetic flux of I-ICMEs in Solar Cycle 24 and so is the radius, but the CCDF of the axial magnetic field intensity is entangled. This means that there are more I-ICMEs with larger total magnetic flux and larger radius in

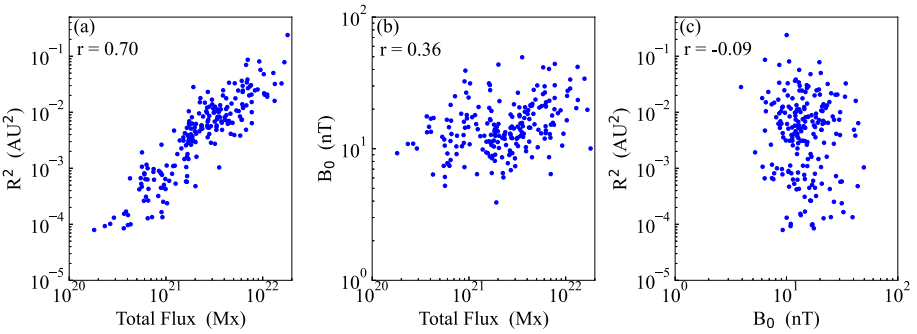

Figure 8 Relationship between total magnetic flux, radius, and axial magnetic field intensity.

Solar Cycle 23 than in Solar Cycle 24. 2) The total magnetic flux and radius of I-ICMEs in Solar Cycles 23 and 24 come from different distribution functions (P-values are 0.064 and 0.036, respectively). 3) The shape of the I-ICMEs total magnetic flux distribution curves for Solar Cycles 23 and 24 is similar, which indicates that the total magnetic flux carried by the ejected CMEs during Solar Cycle 23 is generally a fixed value larger than during Solar Cycle 24. We also discussed the correlation between the total magnetic flux, radius, and axial magnetic field intensity, as shown in Figure 8. Figure 8 shows that the total magnetic flux has a good correlation with the radius square ($r = 0.70$), while the linear correlation with the axial magnetic field intensity is weak ($r = 0.36$). It indicates that I-ICMEs with high total magnetic flux tend to have larger radius, although there is a lot of uncertainty in their axial magnetic field intensities. Panel c shows that the axial magnetic field intensity has almost no correlation with the radius square ($r = -0.09$). This indicates that the magnitude of the axial magnetic field carried by the ICMEs is independent of the radius of the ICMEs. This suggests that the weak magnetic field of ICMEs at 1 AU in Solar Cycle 24 is not caused by the size of the radius of the ICMEs.

3.3. Magnetic Field Strength, Speed, and Dst

Similarly, we also compared the total magnetic field intensity (average value) and the southward magnetic field intensity (maximum) of I-ICMEs and M-ICMEs in Solar Cycles 23 and 24, as shown in Figure 9. We conclude from Table 3 and Figure 9 that for most CME events in Solar Cycles 23 and 24, there is no difference between the total magnetic field and the strength of the southward magnetic field of ICMEs (I-ICMEs and M-ICMEs). Even though, there are more I-ICMEs and M-ICMEs events with stronger southward magnetic field in Solar Cycle 23. The extreme value of the maximum southward magnetic field carried by ICMEs in Solar Cycle 23 is much larger than that in Solar Cycle 24. This is the reason for the difference between the mean values of the total magnetic field and the southward magnetic field in the two solar cycles.

In addition, we also compared the propagation speed of I-ICMEs and M-ICMEs in Solar Cycles 23 and 24 in Table 3 and Figure 10. Figure 10 shows the propagation speed distribution of different types of ICMEs in the two solar cycles. It is not surprising to find that the propagation speed of ICMEs in Solar Cycle 23 is faster than that in Solar Cycle 24. The distribution of speeds also had a significant difference (P-values are 0.0044 and 0.0166, respectively). Interestingly, the I-ICME speed distribution curves of Solar Cycles 23 and 24 are similar in shape, which reflects that the overall I-ICME propagation speeds of Solar Cycle 23 are a certain value larger than those of Solar Cycle 24. The difference in propagation

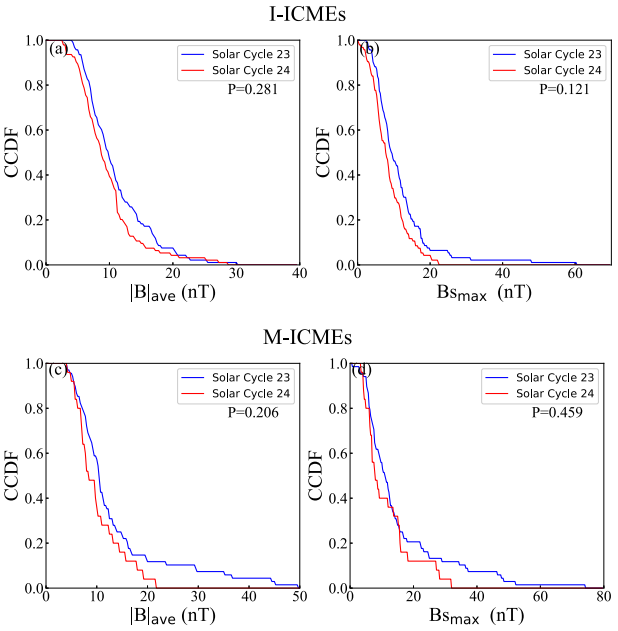

Figure 9 Distribution of the average value of the total magnetic field and the maximum value of the southward magnetic field. The *solid blue line* in the figure represents Solar Cycle 23, while the *red line* represents Solar Cycle 24. The CCDF is a complementary cumulative distribution function and the P-value is the result of the KS test.

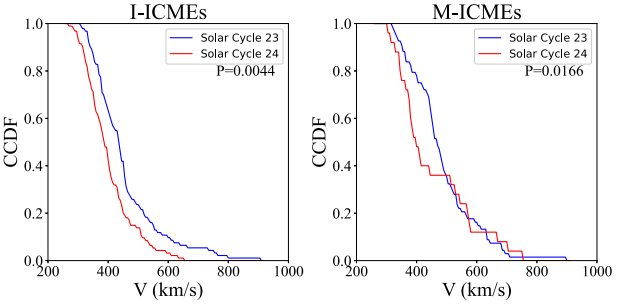

Figure 10 Distribution of the propagation speed of ICMEs in Solar Cycles 23 and 24. The *solid blue line* in the figure represents the Solar Cycle 23, while the *red line* represents the Solar Cycle 24. The CCDF is a complementary cumulative distribution function and the P-value is the result of the KS test.

speed distribution should be caused by the slower speed of the background solar wind in Solar Cycle 24 (Gopalswamy et al., 2015a,b). Figure 11 shows the change of background solar wind speed (according to the time in the ICME list, the background solar wind speed is calculated after removing the ICMEs) from 1996 to 2019. We found that the background solar wind speed of Solar Cycle 23 is faster than that of Solar Cycle 24 (the average values of the two cycles are 440.10 km s^{-1} and 412.51 km s^{-1}, respectively), which is consistent with the study of Hajra et al. (2021). In addition, the white light CME speed distributions in Solar Cycles 23 and 24 are similar (Gopalswamy et al., 2014; Gopalswamy, Tsurutani, and Yan, 2015). These two points explain why ICMEs in Solar Cycle 24 travel slowly. In general, the speed of the CMEs at 1AU is significantly affected by the speed of the background solar wind (Case et al., 2008; Owens, Lockwood, and Barnard, 2020; Temmer et al., 2011; Gopalswamy et al., 2001). The resistance of ICMEs during propagation is proportional to the square of the speed difference between ICMEs and the solar wind (Vršnak and Žic, 2007). There is a greater speed difference in Solar Cycle 24, which indicates that the

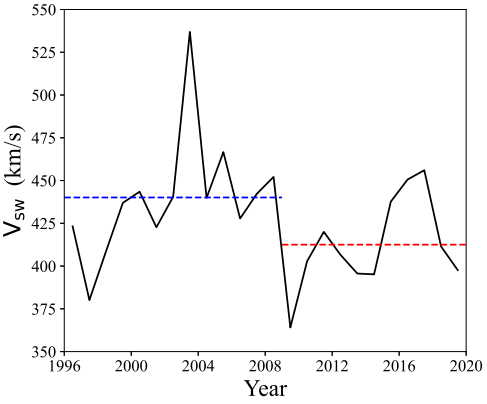

Figure 11 Distribution of the background solar wind speed in Solar Cycles 23 and 24. The *blue dotted line* is the average value of the background solar wind of Solar Cycle 23 and the *red dotted line* is that of Solar Cycle 24.

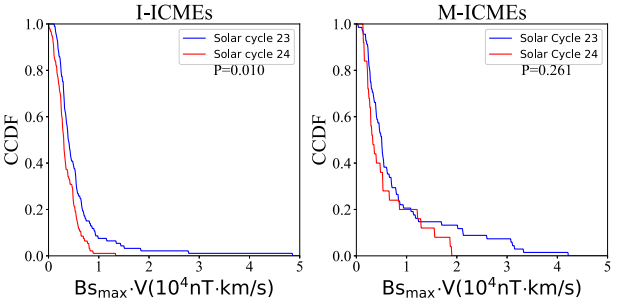

Figure 12 Distribution of $Bs_{max}V$ in Solar Cycles 23 and 24. The *solid blue line* in the figure represents Solar Cycle 23, and the *red line* represents Solar Cycle 24. The CCDF is a complementary cumulative distribution function and the P-value is the result of the KS test.

propagation of CMEs is subject to greater resistance, which also explains why the speed of ICMEs in Solar Cycle 24 is lower.

Dst_{min} is related to the southward magnetic field and propagation speed of ICMEs: $Dst_{min} = -0.01Bs_{max}V - 32$ nT (Gopalswamy, 2008). So we compared the distribution of BsV of I-ICMEs and M-ICMEs, as shown in Figure 12, and counted the number (and frequency) of geomagnetic storms caused by these ICMEs, as shown in Table 4. Figure 12 shows the distribution of $Bs_{max}V$ in Solar Cycles 23 and 24 for I-ICME and M-ICMEs, respectively. According to the P-value of the KS test, the $Bs_{max}V$ parameters for I-ICMEs in Solar Cycles 23 and 24 come from two different distribution functions, while the $Bs_{max}V$ parameters for M-ICMEs come from the same distribution. $D_{crit,\alpha}$ is the critical value of the KS test method at the significance level α, then, due to different number of I-ICMEs and M-ICMEs during the two solar cycles (93 and 94 I-ICMEs and 68 and 25 M-ICMEs, during Solar Cycles 23 and 24, respectively), the calculated critical value $D_{crit,\alpha}$ is different ($D_{crit,\alpha} = \sqrt{-ln(\frac{\alpha}{2})} \times \frac{1}{2} \times \sqrt{\frac{n_{23}+n_{24}}{n_{23}\times n_{24}}}$, $D_{crit,\alpha}$ values are 0.179 and 0.286 in I-ICMEs and M-ICMEs, respectively). The smaller the $D_{crit,\alpha}$ is, the more likely it is that the P-value is less than 0.1. This is why the M-ICME images look different, but according to the KS test there is no significant difference in the distribution. From this figure, we can see that the $Bs_{max}V$ range of ICMEs (I-ICMEs and M-ICMEs) in Solar Cycle 23 is much wider than in Solar Cycle 24, which indicates that the strongest geomagnetic storm in Solar Cycle 23 is indeed stronger than that of Solar Cycle 24, and the probability of a strong geomagnetic storm is greater.

Table 4 shows the number of moderate, strong, and extremely strong geomagnetic storms associated with I-ICMEs and M-ICMEs in Solar Cycles 23 and 24. The total number of I-

Table 4 The number (and frequency) of geomagnetic storms associated with I-ICMEs and M-ICMEs.

	I-ICMEs				
	ICME number	Moderate	Strong	Extremely strong	Total
SC 23	93	28 (30.1%)	23 (24.7%)	4 (4.3%)	55 (59.1%)
SC 24	94	26 (27.7%)	8 (8.5%)	0 (0.0%)	34 (36.2%)
Ratio	0.99	1.08	2.88	—	1.62
	M-ICMEs				
	ICME number	Moderate	Strong	Extremely strong	Total
SC 23	68	8 (11.8%)	19 (27.9%)	7 (10.3%)	34 (50.0%)
SC 24	25	4 (16.0%)	3 (12.0%)	2 (8.0%)	9 (36.0%)
Ratio	2.72	2	6.33	3.5	3.78

Moderate: $-100\ \text{nT} < \text{Dst}_{\text{min}} \leq -50\ \text{nT}$

Strong: $-200\ \text{nT} < \text{Dst}_{\text{min}} \leq -100\ \text{nT}$

Extremely strong: $\text{Dst}_{\text{min}} \leq -200\ \text{nT}$

ICMEs that caused geomagnetic storms in Solar Cycles 23 and 24 is 34 and 55, respectively, as shown in Table 4. Between the two cycles, there are not many differences in the overall number of I-ICMEs or the number of I-ICMEs that caused moderate geomagnetic storms. Solar Cycle 24 has a significantly lower number and percentage of I-ICMEs that generate strong and extremely strong geomagnetic storms than Solar Cycle 23. In terms of M-ICMEs, Solar Cycle 24 has fewer M-ICMEs events (25) than Solar Cycle 23, which had 68 M-ICMEs. Despite the fact that the proportion of M-ICMEs that cause both moderate and extremely strong geomagnetic storms is nearly equal. The number of geomagnetic storms caused by M-ICMEs is significantly lower in Solar Cycle 24 than in Solar Cycle 23.

4. Discussion and Conclusions

In this work, we used the ICME catalogue form 1996 to 2019 to compare the number and key parameters (total magnetic field strength, southward magnetic field strength, propagation speed) of ICMEs in Solar Cycles 23 and 24. We also used the velocity-modified cylindrical force-free flux rope model to fit I-ICMEs of Solar Cycles 23 and 24, and compared the total magnetic flux, radius and axial magnetic field intensity in the fitting parameters. The main results are summarized below.

1. While the number of I-ICMEs in Solar Cycle 23 is comparable to that in Solar Cycle 24, the number of M-ICMEs in Solar Cycle 23 is nearly three times higher than that in Solar Cycle 24. In the two solar cycles, the number of I-ICMEs and M-CMEs that are the most geoeffective is equal in proportion to the total number of I-ICMEs and M-ICMEs. The number of ICMEs with N $\rightarrow$ S and S $\rightarrow$ N is basically the same whether in Solar Cycle 23 or Solar Cycle 24.
2. At 1 AU, the total magnetic flux and radius of I-ICMEs in Solar Cycle 23 are significantly greater than those in Solar Cycle 24, while the axial magnetic field intensity is basically the same. Gopalswamy et al. (2015a) studied magnetic cloud events in the first 73 months of Solar Cycles 23 and 24 and found that the average size of magnetic clouds in Solar Cycle 24 was 23% smaller than in Solar Cycle 23. The time period studied in

our study is 1996-2019, which is longer than Gopalswamy et al. (2015a), but the obtained conclusions are consistent. The total magnetic flux has a good correlation with the square of the radius ($r = 0.70$), while it has a weak correlation with the axial magnetic field strength ($r = 0.36$). The axial magnetic field intensity is almost independent of the square of the radius ($r = -0.09$). This suggests that the weak magnetic field of ICMEs at 1 AU in Solar Cycle 24 is not caused by the radius of the ICMEs.

3. For both I-ICMEs and M-ICMEs, there are no significant differences in the distribution of the maximum southward magnetic field intensity and the total magnetic field intensity during Solar Cycles 23 and 24. However, the speed distribution of I-ICMEs and M-ICMEs shows a significant difference between the two cycles.
4 In Solar Cycles 23 and 24, the probability of M-ICMEs and I-ICMEs causing moderate geomagnetic storms is not significantly different, but the probability of strong geomagnetic storms caused by both I-ICMEs and M-ICMEs is very different. During Solar Cycle 23, the probability of I-ICMEs and M-ICMEs causing strong geomagnetic storms was 24% and 29%, respectively, while during Solar Cycle 24, the probability of I-ICMEs and M-ICMEs causing strong geomagnetic storms was 8% and 13%, respectively. This indicates that the geoeffectiveness of I-ICMEs and M-ICMEs in Solar Cycle 24 is weaker than those in Solar Cycle 23.

Based on the previous comparison and analysis, we believe that the reasons for the weaker geomagnetic activity in Solar Cycle 24 from the perspective of ICMEs are as follows. i) For I-ICMEs, the number of I-ICMEs in Solar Cycles 23 and 24 is basically the same, but the total number of geomagnetic storms varies greatly. This may be due to the slower propagation speed of I-ICMEs and the lack of strong southward magnetic fields in Solar Cycle 24, which makes I-ICMEs to have weaker geoeffectiveness, resulting in a lower number of strong geomagnetic storms (-200 nT $< \mathrm{Dst_{min}} \leq -100$ nT). The lack of extremely strong southward magnetic field events in I-ICMEs leads to no extremely strong geomagnetic storms ($\mathrm{Dst_{min}} \leq -200$ nT). ii) For M-ICMEs, the number of M-ICMEs in Solar Cycle 23 is almost three times that in Solar Cycle 24 and the total number and probability of geomagnetic storms vary greatly. The smaller number of M-ICMEs in Solar Cycle 24 leads to a corresponding decrease in the number of moderate and extremely strong geomagnetic storms. M-ICMEs have lower propagation speed and weaker southward magnetic field during the Solar Cycle 24, resulting in fewer strong geomagnetic storms. In the study of Gopalswamy et al. (2014), they concluded that the decrease in the number of geomagnetic storms is caused by a decrease in the number of energetic coronal mass ejections and a lack of a large Bs component of the interplanetary magnetic field. Gopalswamy et al. (2015a) found that the sharp decrease in VBs may be the main reason for the similar decrease in geomagnetic storm intensity during the Solar Cycle 24. The decrease in speed and Bs resulted in a decrease in VBs. Hajra et al. (2021) concluded that the decrease of interplanetary magnetic field, solar wind plasma speed, and solar wind magnetosphere energy coupling led to the lowest number of geomagnetic storms in Solar Cycle 24. Our results confirm the conclusions obtained from this work.

Acknowledgments We acknowledge the use of data from the *Wind* and the *Advanced Composition Explorer* (ACE) satellites and World Data Center-Sunspot Index and Long-term Solar Observations (WDC-SILSO), Royal Observatory of Belgium, Brussels. We would like to thank the team of Solar-Terrestrial Exploration and Physics (STEP) at the University of Science and Technology of China for providing the ICME list and fitting models. This work is supported by grants from the NSFC (42188101, 42325405, 42130204, 41904151, 42074222) and the Strategic Priority Program of the Chinese Academy of Sciences (XDB41000000).

Author contributions Z. Z., C. S., and Y. C. wrote the main manuscript text. D. M., J. L., M. X., Z. Z., C. W., and Y. W. contributed to discussions and offered revisions suggestions.

Funding This work was supported by grants from the NSFC (42188101, 42325405, 42130204, 41904151, 42074222) and the Strategic Priority Program of the Chinese Academy of Sciences (XDB41000000).

Data Availability The list of interplanetary coronal mass ejections in Solar Cycles 23 and 24 can be obtained from the website http://space.ustc.edu.cn/dreams/wind_icmes/index.php, interplanetary magnetic field and solar wind data are available from *Wind* and the *Advanced Composition Explorer* (ACE) satellites (https://cdaweb.gsfc.nasa.gov/istp_public/). The sunspot number data of version 2.0 can be downloaded from World Data Center-Sunspot Index and Long-term Solar Observations (WDC-SILSO), Royal Observatory of Belgium, Brussels (https://wwwbis.sidc.be/silso/datafiles). The simulation of the velocity-modified cylindrically symmetric force-free flux rope model can be obtained from http://space.ustc.edu.cn/dreams/mc_fitting/.

Declarations

Competing interests The authors declare no competing interests.

References

Aulanier, G.: 2010, What triggers coronal mass ejections? In: *38th COSPAR Scientific Assembly* **38**, 2. ADS.

Burlaga, L.F.: 1988, Magnetic clouds and force-free fields with constant alpha. *J. Geophys. Res.* **93**, 7217. DOI. ADS.

Burlaga, L., Sittler, E., Mariani, F., Schwenn, R.: 1981, Magnetic loop behind an interplanetary shock: Voyager, Helios, and IMP 8 observations. *J. Geophys. Res.* **86**, 6673. DOI. ADS.

Burlaga, L., Berdichevsky, D., Gopalswamy, N., Lepping, R., Zurbuchen, T.: 2003, Merged interaction regions at 1 AU. *J. Geophys. Res.* **108**, 1425. DOI. ADS.

Case, A.W., Spence, H.E., Owens, M.J., Riley, P., Odstrcil, D.: 2008, Ambient solar wind's effect on ICME transit times. *Geophys. Res. Lett.* **35**, L15105. DOI. ADS.

Chi, Y., Shen, C., Wang, Y., Xu, M., Ye, P., Wang, S.: 2016, Statistical study of the interplanetary coronal mass ejections from 1995 to 2015. *Solar Phys.* **291**, 2419. DOI. ADS.

Chi, Y., Zhang, J., Shen, C., Hess, P., Liu, L., Mishra, W., Wang, Y.: 2018, Observational study of an Earth-affecting problematic ICME from STEREO. *Astrophys. J.* **863**, 108. DOI. ADS.

Chi, Y., Scott, C., Shen, C., Barnard, L., Owens, M., Xu, M., Zhang, J., Jones, S., Zhong, Z., Yu, B., Lang, M., Wang, Y., Lockwood, M.: 2021, Modeling the observed distortion of multiple (Ghost) CME fronts in STEREO heliospheric imagers. *Astrophys. J. Lett.* **917**, L16. DOI. ADS.

Cid, C., Hidalgo, M.A., Nieves-Chinchilla, T., Sequeiros, J., Viñas, A.F.: 2002, Plasma and magnetic field inside magnetic clouds: a global study. *Solar Phys.* **207**, 187. DOI. ADS.

Dasso, S., Mandrini, C.H., Schmieder, B., Cremades, H., Cid, C., Cerrato, Y., Saiz, E., Démoulin, P., Zhukov, A.N., Rodriguez, L., Aran, A., Menvielle, M., Poedts, S.: 2009, Linking two consecutive nonmerging magnetic clouds with their solar sources. *J. Geophys. Res.* **114**, A02109. DOI. ADS.

Echer, E., Tsurutani, B.T., Gonzalez, W.D.: 2013, Interplanetary origins of moderate (-100 nT $<$ Dst ≤ -50 nT) geomagnetic storms during solar cycle 23 (1996-2008). *J. Geophys. Res.* **118**, 385. DOI. ADS.

Echer, E., Gonzalez, W.D., Tsurutani, B.T., Gonzalez, A.L.C.: 2008, Interplanetary conditions causing intense geomagnetic storms (Dst ≤ -100 nT) during solar cycle 23 (1996-2006). *J. Geophys. Res.* **113**, A05221. DOI. ADS.

Fadaaq, M., Badruddin, B.: 2021, Study of transient modulation of galactic cosmic rays due to interplanetary manifestations of coronal mass ejections: 2010–2017. *Astrophys. Space Sci.* **366**, 10. DOI. ADS.

Goldstein, H.: 1983, On the field configuration in magnetic clouds. In: *NASA Conf. Pub.* **228**, 731. ADS.

Gonzalez, W.D., Joselyn, J.A., Kamide, Y., Kroehl, H.W., Rostoker, G., Tsurutani, B.T., Vasyliunas, V.M.: 1994, What is a geomagnetic storm? *J. Geophys. Res.* **99**, 5771. DOI. ADS.

Gonzalez, W.D., Echer, E., Clua-Gonzalez, A.L., Tsurutani, B.T.: 2007, Interplanetary origin of intense geomagnetic storms (Dst < -100 nT) during solar cycle 23. *Geophys. Res. Lett.* **34**, L06101. DOI. ADS.

Gonzalez, W.D., Echer, E., Tsurutani, B.T., Clúa de Gonzalez, A.L., Dal Lago, A.: 2011, Interplanetary origin of intense, superintense and extreme geomagnetic storms. *Space Sci. Rev.* **158**, 69. DOI. ADS.

Gopalswamy, N.: 2008, Solar connections of geoeffective magnetic structures. *J. Atmos. Solar-Terr. Phys.* **70**, 2078. DOI. ADS.

Gopalswamy, N., Tsurutani, B., Yan, Y.: 2015, Short-term variability of the Sun-Earth system: an overview of progress made during the CAWSES-II period. *Prog. Earth Planet. Sci.* **2**, 13. DOI. ADS.

Gopalswamy, N., Lara, A., Yashiro, S., Kaiser, M.L., Howard, R.A.: 2001, Predicting the 1-AU arrival times of coronal mass ejections. *J. Geophys. Res.* **106**, 29207. DOI. ADS.

Gopalswamy, N., Akiyama, S., Yashiro, S., Mäkelä, P.: 2010, Coronal mass ejections from sunspot and non-sunspot regions. In: *Magnetic Coupling Between the Interior and Atmosphere of the Sun*, *Astrophys. Space Sci. Proc.* **19**, 289. DOI. ADS.

Gopalswamy, N., Akiyama, S., Yashiro, S., Xie, H., Mäkelä, P., Michalek, G.: 2014, Anomalous expansion of coronal mass ejections during solar cycle 24 and its space weather implications. *Geophys. Res. Lett.* **41**, 2673. DOI. ADS.

Gopalswamy, N., Akiyama, S., Yashiro, S., Xie, H., Makela, P., Michalek, G.: 2015b, The Mild Space Weather in Solar Cycle 24. ArXiv e-prints, arXiv. DOI. ADS.

Gopalswamy, N., Yashiro, S., Xie, H., Akiyama, S., Mäkelä, P.: 2015a, Properties and geoeffectiveness of magnetic clouds during solar cycles 23 and 24. *J. Geophys. Res.* **120**, 9221. DOI. ADS.

Gulisano, A.M., Démoulin, P., Dasso, S., Rodriguez, L.: 2012, Expansion of magnetic clouds in the outer heliosphere. *Astron. Astrophys.* **543**, A107. DOI. ADS.

Hajra, R., Marques de Souza Franco, A., Echer, E., José Alves Bolzan, M.: 2021, Long term variations of the geomagnetic activity: a comparison between the strong and weak solar activity cycles and implications for the space climate. *J. Geophys. Res.* **126**, e28695. DOI. ADS.

Hidalgo, M.A., Nieves-Chinchilla, T.: 2012, A global magnetic topology model for magnetic clouds. I. *Astrophys. J.* **748**, 109. DOI. ADS.

Hidalgo, M.A., Nieves-Chinchilla, T., Cid, C.: 2002, Elliptical cross-section model for the magnetic topology of magnetic clouds. *Geophys. Res. Lett.* **29**, 1637. DOI. ADS.

Hidalgo, M.A., Cid, C., Vinas, A.F., Sequeiros, J.: 2002, A non-force-free approach to the topology of magnetic clouds in the solar wind. *J. Geophys. Res.* **107**, 1002. DOI. ADS.

Hu, Q., Sonnerup, B.U.Ö.: 2002, Reconstruction of magnetic clouds in the solar wind: orientations and configurations. *J. Geophys. Res.* **107**, 1142. DOI. ADS.

Janvier, M., Démoulin, P., Dasso, S.: 2013, Global axis shape of magnetic clouds deduced from the distribution of their local axis orientation. *Astron. Astrophys.* **556**, A50. DOI. ADS.

Klein, L.W., Burlaga, L.F.: 1982, Interplanetary magnetic clouds at 1 AU. *J. Geophys. Res.* **87**, 613. DOI. ADS.

Kumar, A., Rust, D.M.: 1996, Interplanetary magnetic clouds, helicity conservation, and current-core flux-ropes. *J. Geophys. Res.* **101**, 15667. DOI. ADS.

Larson, D.E., Lin, R.P., McTiernan, J.M., McFadden, J.P., Ergun, R.E., McCarthy, M., Rème, H., Sanderson, T.R., Kaiser, M., Lepping, R.P., Mazur, J.: 1997, Tracing the topology of the October 18-20, 1995, magnetic cloud with $\sim$0.1-10^2 keV electrons. *Geophys. Res. Lett.* **24**, 1911. DOI. ADS.

Lepping, R.P., Jones, J.A., Burlaga, L.F.: 1990, Magnetic field structure of interplanetary magnetic clouds at 1 AU. *J. Geophys. Res.* **95**, 11957. DOI. ADS.

Lepping, R.P., Wu, C.-C., Berdichevsky, D.B.: 2005, Automatic identification of magnetic clouds and cloud-like regions at 1 AU: occurrence rate and other properties. *Ann. Geophys.* **23**, 2687. DOI. ADS.

Lepping, R.P., Berdichevsky, D.B., Wu, C.-C., Szabo, A., Narock, T., Mariani, F., Lazarus, A.J., Quivers, A.J.: 2006, A summary of WIND magnetic clouds for years 1995-2003: model-fitted parameters, associated errors and classifications. *Ann. Geophys.* **24**, 215. DOI. ADS.

Lugaz, N., Manchester, I.W.B., Gombosi, T.I.: 2005, Numerical simulation of the interaction of two coronal mass ejections from sun to Earth. *Astrophys. J.* **634**, 651. DOI. ADS.

Lugaz, N., Temmer, M., Wang, Y., Farrugia, C.J.: 2017, The interaction of successive coronal mass ejections: a review. *Solar Phys.* **292**, 64. DOI. ADS.

Marubashi, K.: 1986, Structure of the interplanetary magnetic clouds and their solar origins. *Adv. Space Res.* **6**, 335. DOI. ADS.

Marubashi, K., Lepping, R.P.: 2007, Long-duration magnetic clouds: a comparison of analyses using torus- and cylinder-shaped flux rope models. *Ann. Geophys.* **25**, 2453. DOI. ADS.

Mierla, M., Inhester, B., Antunes, A., Boursier, Y., Byrne, J.P., Colaninno, R., Davila, J., de Koning, C.A., Gallagher, P.T., Gissot, S., Howard, R.A., Howard, T.A., Kramar, M., Lamy, P., Liewer, P.C., Maloney, S., Marqué, C., McAteer, R.T.J., Moran, T., Rodriguez, L., Srivastava, N., St. Cyr, O.C., Stenborg, G., Temmer, M., Thernisien, A., Vourlidas, A., West, M.J., Wood, B.E., Zhukov, A.N.: 2010, On the 3-D reconstruction of coronal mass ejections using coronagraph data. *Ann. Geophys.* **28**, 203. DOI. ADS.

Mulligan, T., Russell, C.T.: 2001, Multispacecraft modeling of the flux rope structure of interplanetary coronal mass ejections: cylindrically symmetric versus nonsymmetric topologies. *J. Geophys. Res.* **106**, 10581. DOI. ADS.

Mustajab, F., Badruddin: 2011, Geoeffectiveness of the interplanetary manifestations of coronal mass ejections and solar-wind stream-stream interactions. *Astrophys. Space Sci.* **331**, 91. DOI. ADS.

Owens, M.J., Lockwood, M., Barnard, L.A.: 2020, The value of CME arrival time forecasts for space weather mitigation. *Space Weather* **18**, e02507. DOI. ADS.

Plunkett, S.P., Thompson, B.J., St. Cyr, O.C., Howard, R.A.: 2001, Solar source regions of coronal mass ejections and their geomagnetic effects. *J. Atmos. Solar-Terr. Phys.* **63**, 389. DOI. ADS.

Qiu, S., Zhang, Z., Yousof, H., Soon, W., Jia, M., Tang, W., Dou, X.: 2022, The interplanetary origins of geomagnetic storm with $Dst_{min} \leq -50$ nT during solar cycle 24 (2009-2019). *Adv. Space Res.* **70**, 2047. DOI. ADS.

Rawat, R., Echer, E., Gonzalez, W.D.: 2018, How different are the solar wind-interplanetary conditions and the consequent geomagnetic activity during the ascending and early descending phases of the solar cycles 23 and 24? *J. Geophys. Res.* **123**, 6621. DOI. ADS.

Richardson, I.G., Cane, H.V.: 2012, Solar wind drivers of geomagnetic storms during more than four solar cycles. *J. Space Weather Space Clim.* **2**, A01. DOI. ADS.

Romashets, E.P., Vandas, M.: 2003, Force-free field inside a toroidal magnetic cloud. *Geophys. Res. Lett.* **30**, 2065. DOI. ADS.

Russell, C.T., Shinde, A.A., Jian, L.: 2005, A new parameter to define interplanetary coronal mass ejections. *Adv. Space Res.* **35**, 2178. DOI. ADS.

Shen, C., Wang, Y., Pan, Z., Miao, B., Ye, P., Wang, S.: 2014, Full-halo coronal mass ejections: arrival at the Earth. *J. Geophys. Res.* **119**, 5107. DOI. ADS.

Shen, C., Chi, Y., Wang, Y., Xu, M., Wang, S.: 2017, Statistical comparison of the ICME's geoeffectiveness of different types and different solar phases from 1995 to 2014. *J. Geophys. Res.* **122**, 5931. DOI. ADS.

Shen, C., Xu, M., Wang, Y., Chi, Y., Luo, B.: 2018, Why the shock-ICME complex structure is important: learning from the early 2017 September CMEs. *Astrophys. J.* **861**, 28. DOI. ADS.

Shen, C., Chi, Y., Xu, M., Wang, Y.: 2021, Origination of extremely intense south component of magnetic field (B_s) in the ICME. *Frontiers Phys.* **9**, 673. DOI. ADS.

Temmer, M., Rollett, T., Möstl, C., Veronig, A.M., Vršnak, B., Odstrčil, D.: 2011, Influence of the ambient solar wind flow on the propagation behavior of interplanetary coronal mass ejections. *Astrophys. J.* **743**, 101. DOI. ADS.

Vandas, M., Romashets, E.P.: 2003, A force-free field with constant alpha in an oblate cylinder: a generalization of the lundquist solution. *Astron. Astrophys.* **398**, 801. DOI. ADS.

Vourlidas, A.: 2014, The flux rope nature of coronal mass ejections. *Plasma Phys. Control. Fusion* **56**, 064001. DOI. ADS.

Vršnak, B., Žic, T.: 2007, Transit times of interplanetary coronal mass ejections and the solar wind speed. *Astron. Astrophys.* **472**, 937. DOI. ADS.

Wang, Y.M., Ye, P.Z., Wang, S.: 2003, Multiple magnetic clouds: several examples during March-April 2001. *J. Geophys. Res.* **108**, 1370. DOI. ADS.

Wang, Y.M., Ye, P.Z., Wang, S., Zhou, G.P., Wang, J.X.: 2002, A statistical study on the geoeffectiveness of Earth-directed coronal mass ejections from March 1997 to December 2000. *J. Geophys. Res.* **107**, 1340. DOI. ADS.

Wang, Y., Zheng, H., Wang, S., Ye, P.: 2005, MHD simulation of the formation and propagation of multiple magnetic clouds in the heliosphere. *Astron. Astrophys.* **434**, 309. DOI. ADS.

Wang, Y., Zhou, Z., Shen, C., Liu, R., Wang, S.: 2015, Investigating plasma motion of magnetic clouds at 1 AU through a velocity-modified cylindrical force-free flux rope model. *J. Geophys. Res.* **120**, 1543. DOI. ADS.

Webb, D.F., Howard, R.A.: 1994, The solar cycle variation of coronal mass ejections and the solar wind mass flux. *J. Geophys. Res.* **99**, 4201. DOI. ADS.

Xu, M., Shen, C., Wang, Y., Luo, B., Chi, Y.: 2019, Importance of shock compression in enhancing ICME's geoeffectiveness. *Astrophys. J. Lett.* **884**, L30. DOI. ADS.

Xue, X.H., Wang, Y., Ye, P.Z., Wang, S., Xiong, M.: 2005, Analysis on the interplanetary causes of the great magnetic storms in solar maximum (2000 2001). *Planet. Space Sci.* **53**, 443. DOI. ADS.

Yermolaev, Y.I., Lodkina, I.G., Dremukhina, L.A., Yermolaev, M.Y., Khokhlachev, A.A.: 2021, What solar-terrestrial link researchers should know about interplanetary drivers. *Universe* **7**, 138. DOI. ADS.

Zhang, G., Burlaga, L.F.: 1988, Magnetic clouds, geomagnetic disturbances, and cosmic ray decreases. *J. Geophys. Res.* **93**, 2511. DOI. ADS.

Zhang, J., Dere, K.P., Howard, R.A., Bothmer, V.: 2003, Identification of solar sources of major geomagnetic storms between 1996 and 2000. *Astrophys. J.* **582**, 520. DOI. ADS.

Zhang, J., Richardson, I.G., Webb, D.F., Gopalswamy, N., Huttunen, E., Kasper, J.C., Nitta, N.V., Poomvises, W., Thompson, B.J., Wu, C.-C., Yashiro, S., Zhukov, A.N.: 2007, Solar and interplanetary sources of major geomagnetic storms ($Dst \leq -100$ nT) during 1996-2005. *J. Geophys. Res.* **112**, A10102. DOI. ADS.

Zhang, J., Temmer, M., Gopalswamy, N., Malandraki, O., Nitta, N.V., Patsourakos, S., Shen, F., Vršnak, B., Wang, Y., Webb, D., Desai, M.I., Dissauer, K., Dresing, N., Dumbović, M., Feng, X., Heinemann, S.G., Laurenza, M., Lugaz, N., Zhuang, B.: 2021, Earth-affecting solar transients: a review of progresses in solar cycle 24. *Prog. Earth Planet. Sci.* **8**, 56. DOI. ADS.